Hindawi
Geofluids
Volume 2021, Article ID 6657662, 13 pages
https://doi.org/10.1155/2021/6657662

Research Article

Permeability of Sand-Based Cemented Backfill under Different Stress Conditions: Effects of Confining and Axial Pressures

Cunli Zhu,[1,2] **Jixiong Zhang**,[1,2] **Nan Zhou**,[1,2] **Meng Li**,[1,2] **and Yaben Guo**[1,2]

[1]*School of Mines, China University of Mining and Technology, Xuzhou, 221116 Jiangsu, China*
[2]*State Key Laboratory of Coal Resources and Safe Mining, Xuzhou, 221116 Jiangsu, China*

Correspondence should be addressed to Nan Zhou; tb18020034b1@cumt.edu.cn

Received 13 December 2020; Revised 22 January 2021; Accepted 5 February 2021; Published 20 February 2021

Academic Editor: Guanglei Zhang

Sand-based cemented backfill (SBCB) mining technology is instrumental in utilizing coal resources buried under the water bodies. SBCB is exposed to the long-term action of mining-induced stresses in the goaf and groundwater permeating via microcracks along the rock strata. Studying the permeability evolution of SBCB under varying stress states is crucial for protecting coal and water resources below the aquifer. This study is focused on the influence law of different stress states on the SBCB permeability exposed to groundwater, which was tested under different axial and confining pressures using a laboratory seepage meter, particle size analyzer, scanning electron microscope (SEM), and X-ray diffractometer (XRD). Best-fitting quadratic polynomials linking the SBCB permeability with confining and axial pressures, respectively, were obtained via statistical processing of test results. The permeability gradually dropped within the elastic range as the confining and axial pressures increased. Moreover, an increase in the confining pressure caused a more dramatic reduction in the SBCB permeability than the axial pressure. Finally, the SBCB seepage mechanism under different stress states was revealed based on the particle size analysis, XRD patterns, and SEM microstructure. These findings are considered instrumental in substantiating safe mining of coal resources below the water bodies and above the confined groundwater.

1. Introduction

Most developed countries have limited oil and gas resources, which are imported or gradually replaced by green energy sources. China follows this trend and takes advantage of its abundant coal resources, in which share in the national primary energy consumption in 2020 exceeded 60% and is expected to remain high in the foreseeable future. In China, the occurrence conditions of coal resources are complex and highly variable. Most coal resources are located below the water bodies and above the confined groundwater [1–3]. Coal resources threatened by water account for over 27% of the total proven coal reserves. Waterproof coal pillars of large scale need to be left to mine these coal resources using the conventional methods [4, 5]. This implies considerable losses of the coal resources and, more importantly, the hidden danger of water burst of coal and rock masses and damage to the aquifer [6–8]. Figure 1(a) shows a transient fracture belt formed due to the rock strata's damage under the conventional mining conditions, resulting in the aquifer's damage.

Given this, some scholars have proposed backfilling and replacement to liberate the coal resources below the water bodies and above the confined groundwater [9–11]. Backfilling materials with high compaction and low permeability are usually needed to ensure the reliability of backfill mining. The sand-based cemented backfill (SBCB) method is a mining technology with small ecological and environmental damage [12–14]. SBCB has high compactness and good control against overlying strata deformation. This method has been extensively applied to the "three-under" coal resources in recent years [15–17]. Figure 1(b) shows the mine water's occurrence state via the SBCB method. The SBCB is made of fly ash, aeolian sand, and cement. Fly ash, as the product

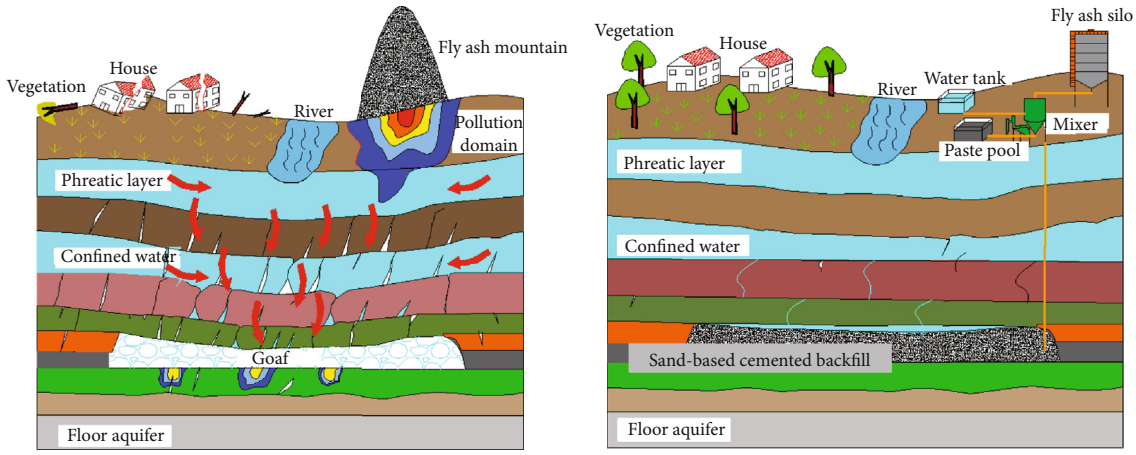

(a) Conventional mining method

(b) Mining method with sand-based cemented backfill

Figure 1: Occurrence state of mine water under different mining methods.

of coal burning, may accumulate in large quantities on the ground surface. Making backfill aggregates with fly ash helps prevent its rainfall erosion, which otherwise carries many noxious elements underground, polluting the soil and groundwater resources [18–20]. Thus, the SBCB turns wastes into resources. Solid wastes, namely, fly ash and aeolian sand, are used for backfilling the goaf to liberate the coal resources, thereby increasing the economic benefit of the coal mine and protecting the environment [21, 22]. However, the aquifer's water may penetrate the roof strata and permeate, via the cracks, into the SBCB in the goaf. As a result, the SBCB is exposed to water [23]. As time progresses and the working face advances, water in the backfilled space invades the backfilling materials, deteriorating their strength. This phenomenon will affect the SBCB stability and control the aquifer and overlying strata deformation [24, 25]. In engineering practice, there is no assurance of whether the SBCB is eroded by groundwater and how the backfill changes permeability under different stress states.

Many studies have been conducted worldwide regarding SBCB permeability. Thus, Liu et al. [26] performed indoor triaxial seepage tests and analyzed the cracked backfill's permeability and strength features. They obtained the failure mode of the cracked sandstone backfill. Mamaghanian et al. [27] carried out a permeability study of a composite material similar to cemented backfill. They elaborated four different permeability models describing the observed patterns, which clarified the studied composite material's permeation performance under different pressures. Hou et al. [28] introduced a damage model and determined the damage evolution features of the prefabricated cracked backfill under the seepage-stress coupling effect. The above studies represent some of the preliminary explorations of the permeability of cemented backfills. However, most of them were concerned with the mechanical performance and model evaluations of the cemented backfill or provided the comparative analysis of permeability variation after modifying the cemented backfill. Very few of them examined evolutionary laws of the SBCB permeability.

Others have investigated the stress state effect on the permeability of concrete and rock strata. Santos and Barros [29] proposed a method for calculating the pressure imposed by the cemented backfill on the retaining wall under a high water level. They concluded that the ground pressure on the retaining wall was caused by water seepage in part of the soil bodies. Hou et al. [30] analyzed the seepage-stress coupling effect on the mechanical behavior, damage evolution law, and the microscopic structural response of cracked cemented gangue-fly ash backfill (CGFB). Barros and Santos [31] provided a numerical simulation of water permeation of soil bodies based on the boundary element method. They calculated the internal friction angle of soil and the inclined angle of the wall surface and plotted the variation diagram of ground pressure coefficient with seepage. Zhang et al. [32] analyzed the influence of confining pressure on permeability characteristics of granite and cracked slate. They clarified the effect of crack morphology on the permeation mechanism of different rock types. Zhou et al. [33] built a theoretical model quantifying the effects of crack-pore permeability coupling and hydromechanical coupling on soft rocks' damage behavior. The above studies of the stress state effect on permeability characteristics were mostly focused on the fractured confining rocks. However, few of them investigated SBCBs exposed to groundwater for a long period under different stress states.

This study is aimed at clarifying the stress state effect (which occurs at different burial depths) on the permeability of SBCB, which is mainly composed of aeolian sand, fly ash, cement, and water. Aeolian sand is used as aggregate, and fly ash and cement are used as binding materials. During hydration reaction, the smaller fly ash and cement particles fill the pores between the aeolian particles, enhancing the overall compaction and antiseepage performance of the SBCB. However, there are scarce data on the permeability variation pattern under different stress states for the SBCB long-term exposure to a moist goaf, which is depicted in Figure 1(b).

(a) Aeolian sand (b) Fly ash (c) Portland cement

Figure 2: Raw materials.

The current study explored the influence of axial pressure and confining pressure on the permeation performance of the SBCB exposed to the long-term action of groundwater. A seepage meter was used to measure the SBCB permeability under the above conditions, while the backfill microstructure was examined via an FEI Quanta 250 scanning electron microscope (SEM) and X-ray diffractometer (XRD). The performed single-factor analysis and the 2-factor 3-level orthogonal experiment revealed the influence of single factors and the combined effect of multiple factors on the SBCB permeation mechanism. The research findings are considered instrumental in substantiating the protection measures for mining under water bodies and ensuring green, safe mining of coal resources under the same type's geological conditions.

2. Materials and Methods

2.1. Test Materials. The raw materials used in the experiments were aeolian sand, fly ash, cement, and water. Aeolian sand and fly ash were collected from the superficial deposits in Yulin City, solid wastes generated by the Yulin Power Station (Shaanxi Province of China). The ordinary Portland cement was acquired from the Jinniu Coal Mine in Yulin City. Photos of raw materials for the experiment are presented in Figure 2, while their particle size distribution and XDR patterns are depicted in Figures 3 and 4, respectively.

2.1.1. Aeolian Sand. Aeolian sand usually serves as an aggregate of the cemented paste. Its particle size distribution and mineral composition play a decisive role in the SBCB's permeability. Figures 3(a) and 4(a) show the particle size distribution and the major mineral components of aeolian sand, respectively. As shown in Figure 3(a), the particle size of aeolian sand ranged between 168 and 571 μm, with an average value of 346.49 μm. The particle size of aeolian sand was small and evenly distributed. When used as an aggregate, the aeolian sand was conducive to enhancing the SBCB's compaction. According to the XRD patterns of the aeolian sand in Figure 4(a), the aeolian sand contained a large amount of quartz, feldspar, and calcite. Quartz existing in large quantities enhanced the SBCB's stability, improving the backfill's compressive resistance and optimizing its bearing capacity.

2.1.2. Fly Ash. Fly ash is usually applied as the binding material in the sand-based cemented paste. Figure 3(b) shows the particle size distribution of fly ash, ranging between 19 and 126 μm, with an average value of 64.683 μm. Therefore, the fly ash is conducive to the SBCB delivery. As indicated by the XRD patterns in Figure 4(b), fly ash contained many quartz and mullite but little muscovite. Chemically stable quartz improved the stability of the SBCB exposed to groundwater.

2.1.3. Cement. Ordinary Portland cement, which is generally a binding material, undergoes hydration reaction in the cemented paste. It is an important raw material for improving the strength and stability of the SBCB. Figure 3(c) shows the particle size distribution of cement, ranging between 6.9 and 99.3 μm, with an average value of 44.846 μm. Smaller particles usually have a more extensive contact area in the SBCB, thereby ensuring a complete hydration reaction. Figure 4(c) shows the XRD pattern of cement, which was rich in calcium silicate ($3CaO{\bullet}SiO_2$) and calcium carbonate and where dicalcium silicate was most abundant. Hydration of these minerals would significantly improve the SBCB strength.

2.2. Test Method

2.2.1. Seepage System. A seepage system of the cemented backfill was designed and constructed by the authors to analyze the stress state effect on the SBCB's permeability. This system consisted of the axial loading subsystem, seepage meter, confining pressure loading subsystem, hydraulic loading subsystem, and data monitoring subsystem. Figure 5 presents a schematic of the seepage system.

(1) Axial Loading System. A WAW-1000D series servohydraulic testing machine incorporated into the axial loading system was used to generate different stresses in the SBCB

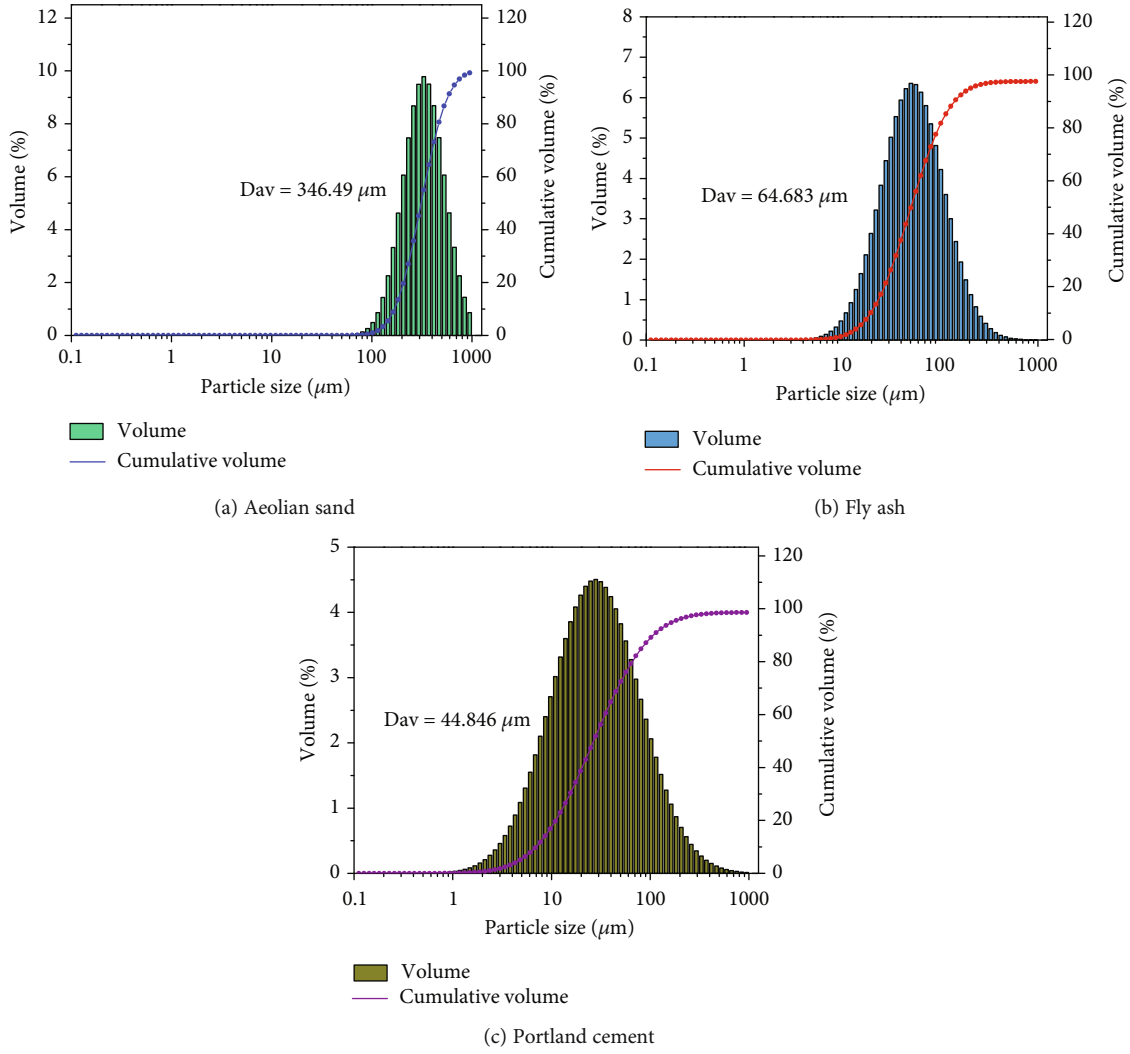

Figure 3: Particle size distributions.

specimens. The maximum stroke of the servohydraulic testing machine was 250 mm, the loading rate was 0.2 mm/min, the display precision grade was 0.5, and the measuring range was 0~1000 kN.

(2) Hydraulic Loading System. The hydraulic loading system applied a seepage pressure to the SBCB. An ultra-high-pressure hydraulic pump was used to apply hydraulic loading. The hydraulic loading system consisted of a water tank, an energy accumulator, a wobble pump for pressure testing, a stop valve, a pressure gauge, and a pressure transmitter.

(3) Confining Pressure Loading System. The confining pressure loading system applied a constant confining pressure on the SBCB. This system ensured the water seepage into SBCB specimens and guaranteed the test reliability. A YE2-100L2-4 three-phase asynchronous motor drove the confining pressure loading system. The hydraulic oil was pumped into the seepage meter to apply a constant confining pressure to the specimens. The power was 3 kW, the frequency was 50 Hz, and the rotational speed was 1420 r/min, which satisfied the test requirements.

(4) Seepage Meter. The seepage meter was the core part of the entire experiment. The seepage meter was composed of the base, tank body, cap, upper press head, lower press head, and porous plate. The entire seepage process of the backfill specimens mainly proceeded in the seepage meter. Figure 6 shows photos of the seepage meter and its components.

(5) Data Collection and Monitoring System. During the seepage system's experimental process, the data were collected and recorded by combining the pressure transmitter with the paperless recorder. The paperless recorder monitored water pressure variations in the water tank over time. The permeability k_D of the backfill specimens was calculated as follows:

$$k_D = \frac{c_f B H \mu}{2 t_f A} \ln \frac{J_0}{J} = \frac{c_f B H \mu}{2 t_f A} \ln \left(\frac{p_{10} - p_{20}}{p_{1f} - p_{2f}} \right), \quad (1)$$

where P_{10} and P_{20} are the initial pressures; P_{1f} and P_{2f} are pressures at time t; J is the pressure gradient at time t; c_f is the compressibility factor of the liquid; B is the water tank

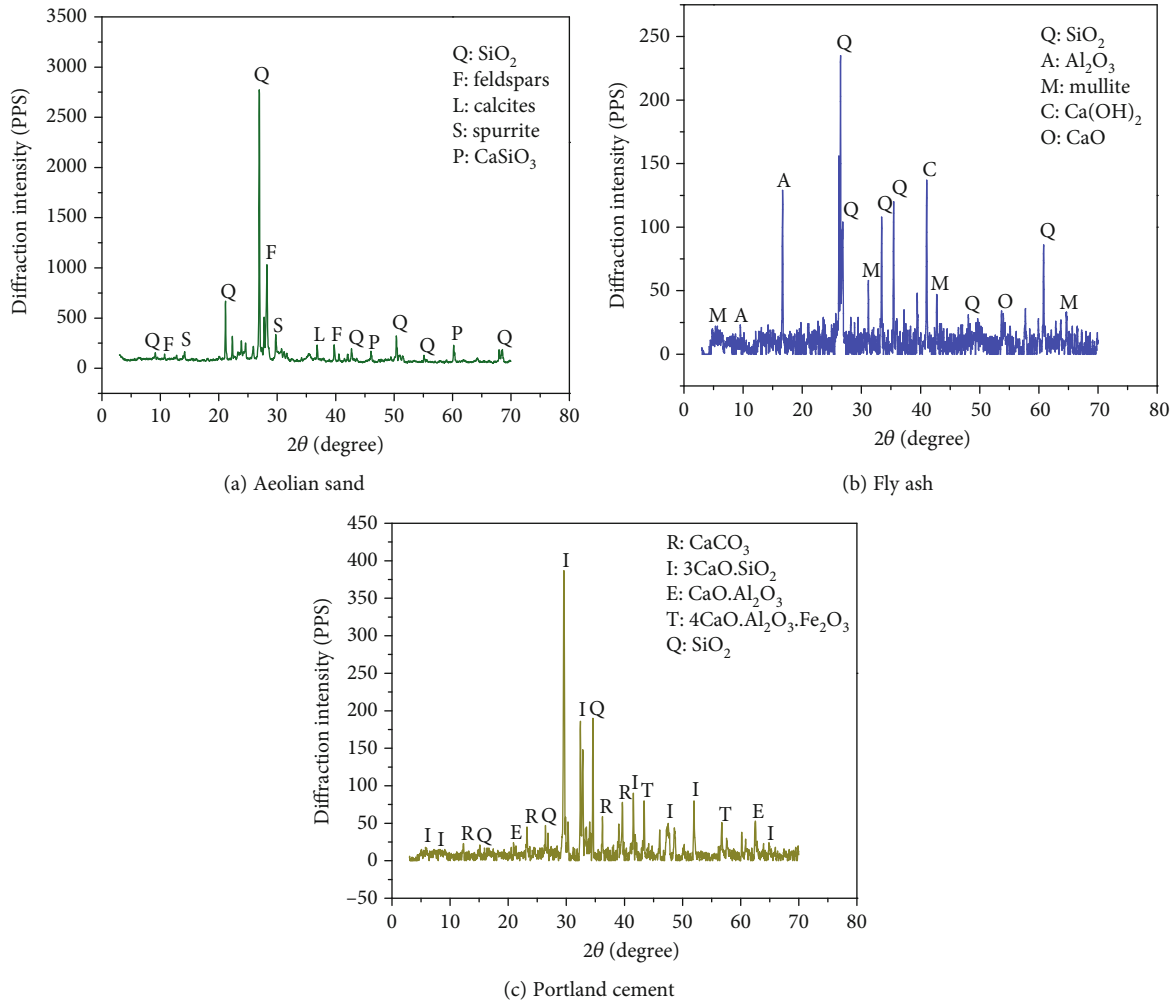

(a) Aeolian sand

(b) Fly ash

(c) Portland cement

Figure 4: XRD patterns of raw materials.

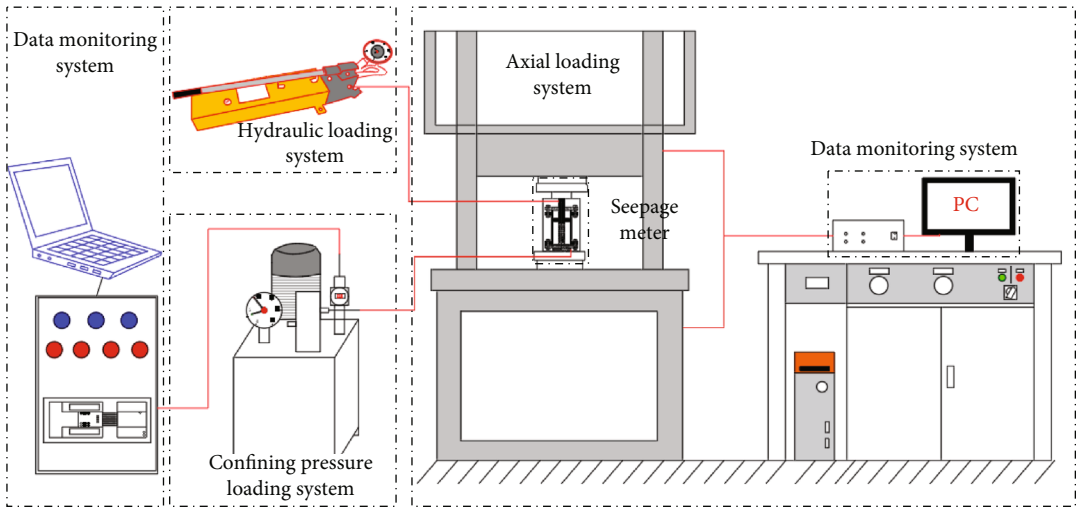

Figure 5: Schematic of the seepage system.

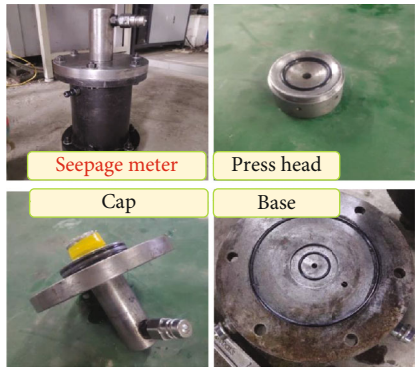

Figure 6: Photos of the seepage meter and its components.

volume; H is the specimen's height; μ is the dynamic viscosity of the seeping liquid; t is the time needed for the experiment; and A is the specimen cross-sectional area.

2.2.2. Microstructural Analysis. An FEI Quanta 250 SEM introduced by the Advanced Analysis and Computation Center of the China University of Mining and Technology was used for the microstructural analysis, as shown in Figure 7(a) An X-ray diffractometer was used to analyze the mineral composition of the raw materials. As shown in Figure 7(b), the X-ray diffractometer was composed of a sealed-tube X-ray source and an X-ray high-voltage generator for precise measuring of specimens' mineral composition.

2.2.3. Test Procedures. The test procedures included the following: determination of physical and chemical properties of raw materials, determination of the mix ratio of each component of the SBCB, preparation and pretreatment of specimens, and the seepage test of pretreated specimens using a WAW-1000D series servohydraulic testing machine. The effect of different stress states on the SBCB's permeability was analyzed based on the experimental results. The SBCB microstructure was observed via the SEM. The experimental workflow is depicted in Figure 8.

As seen in Figure 8, the particle size, chemical composition, and microstructure of the raw materials were first analyzed using the particle size analyzer, XRD, and SEM, respectively. After testing, the cemented paste was prepared by mixing fly ash, aeolian sand, cement, and water at a certain mix ratio according to the GB/T50080-2016 standard for the test method on the performance of ordinary fresh concrete. The paste was poured into a mold with a diameter of 50 mm and a height of 100 mm. The mold was gently shaken for 10-15 s to remove air bubbles from the paste. The paste was left to stand for 8 h and then removed from the mold. The specimen was then cured in a curing box for 28 d under a humidity of 95% and a temperature of $20 \pm 2^{\circ}$C.

According to the GB50218-94 standard for the test method of engineering rock masses, the cured specimens were prepared into standard specimens. A seepage experiment of SBCB was performed under different stress states according to the GB/T23561.12-2010 method for determining physicomechanical properties. After the seepage experiment, the specimens were dried for 12 h in a drying oven at 40°C to prepare them for microstructural analysis. The dried specimens were cut into a length of 10 mm, a width of 10 mm, and a height of 5 mm. Specimens were gold-sprayed to improve the electrical conductivity and hence facilitate the SEM observation. Finally, the effect of different stress states on the SBCB permeability under different stress states was analyzed based on the experimental results.

2.3. Experimental Scheme

2.3.1. Specimen Pretreatment. The specimens were cured for 28 d and then taken out. Each specimen was truncated to a height of 100 mm with a cutting machine. Next, the specimen's two end surfaces were ground flat with a polishing machine to ensure a flatness below 0.5 mm. The parallelism between the two end surfaces was below 0.02 mm. The specimens' machining precision was measured and satisfied the GB 50218-1994 standard for engineering classification of rock masses. The machined specimens were then soaked into the water to saturate them before the seepage test.

2.3.2. Variation Laws of SBCB Permeability under Different Confining Pressures. The aeolian sand mass was a fixed value, and the doping amount of other ingredients was expressed as their mass ratio to that of the aeolian sand. The raw materials' mix ratios for the SBCB preparation were as follows: the fly ash with a mass fraction of 78% accounted for 70%, and the cement for 15%. Secondly, after the dry material was evenly stirred, water was added slowly until its amount required by the mixing ratio was reached. The standard specimens of SBCB were prepared under this mixed ratio [32]. The axial pressure was fixed at 2.5 MPa, and different levels of confining pressure were set up at 1, 2, 3, and 4 MPa [34]. The S1, S5, S6, and S7 tests described in Table 1 were carried out. The variation rules of SBCB permeability under different confining pressures and constant axial pressures were identified.

2.3.3. Variation Rules of Permeability of SBCB under Different Axial Pressures. For standard specimens, the confining pressure was fixed at 3 MPa, while different axial pressures were set up at 2.5, 3.5, 4.5, and 5.5 MPa [34]. Tests S1, S2, S3, and S4 described in Table 1 were carried out. The variation rules of SBCB permeability under different axial pressures and constant confining pressures.

The 2-factor 3-level orthogonal experiment was designed, as shown in Table 1, to study the effect of different axial and confining pressures on the SBCB's permeability.

3. Experimental Results

3.1. Influence Rules of Confining Pressure on the SBCB Permeability. The constant axial pressure of 2.5 MPa was applied, while varying the confining pressures (1, 2, 3, and 4 MPa) to study the influence of a single factor on the SBCB permeability. Each group contained three specimens, and the average permeability value was taken of the three specimens. Table 2 shows the results of the permeability tests.

Figure 9(a) shows the best-fitting curve of the SBCB permeability under four different confining pressures. The

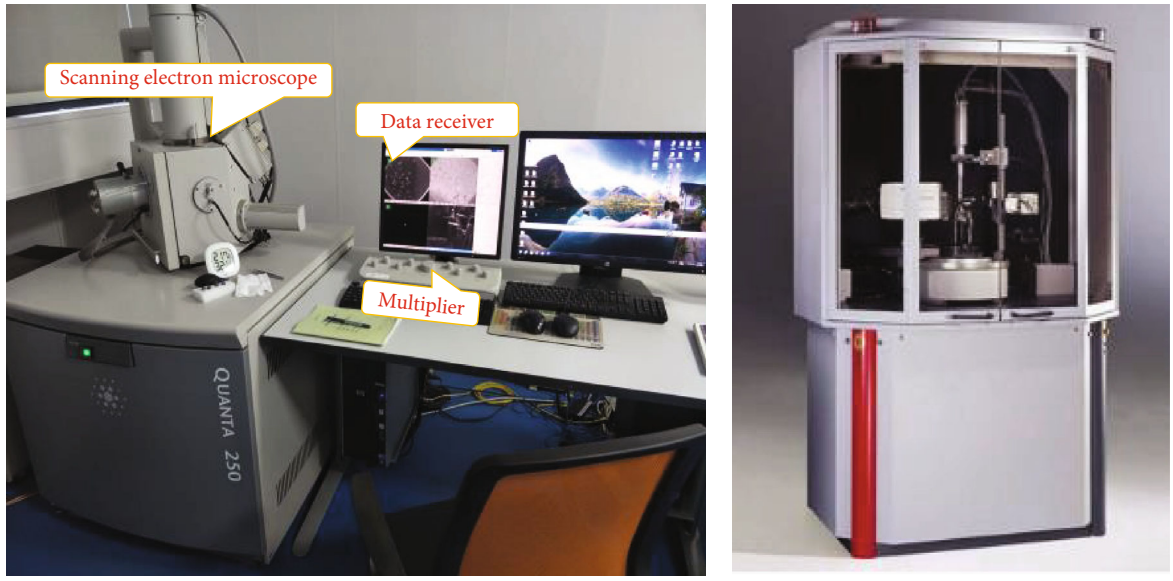

(a) Scanning electron microscope (SEM)

(b) X ray diffractometer (XRD)

Figure 7: Equipment used for microstructural analysis.

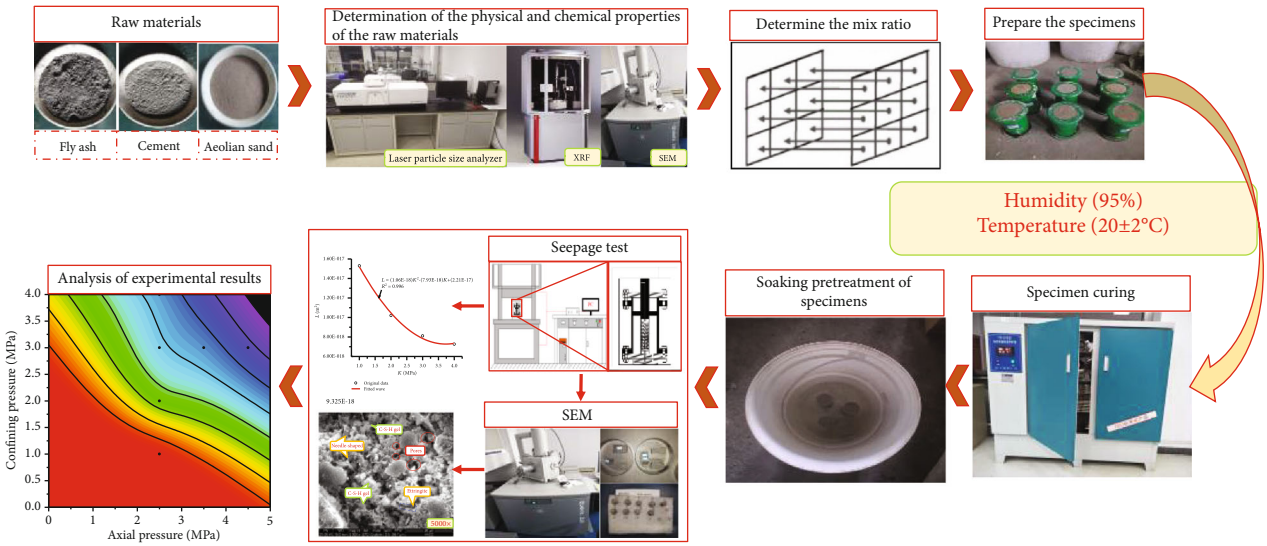

Figure 8: Experimental workflow.

Table 1: Orthogonal experiment design for the SBCB permeability under different stress states.

Experiment No.	Axial pressure (MPa)	Confining pressure (MPa)
S1	2.5	3.0
S2	3.5	3.0
S3	4.5	3.0
S4	5.5	3.0
S5	2.5	1.0
S6	2.5	2.0
S7	2.5	4.0

permeability was related to the confining pressure via a quadratic polynomial, in which equation and correlation coefficient $R^2 = 0.996$ are presented in Figure 9(a). As the confining pressure increased, the permeability decreased at a progressively slowing rate. As the confining pressure grew from 1 to 4 MPa, the permeability dropped from 1.53×10^{-17} to 7.26×10^{-18} m^2, i.e., by 52.5%. This was due to initially small confining pressure in the backfill, which still had pores to form seepage channels, leading to a higher permeability. But as the confining pressure increased, the pores inside the backfill were closed under compaction. The seepage channels were closed as well. Therefore, the permeability gradually decreased at a progressively slowing rate.

Table 2: Results of SBCB permeability tests under different confining pressures.

Axial pressure (MPa)	Confining pressure (MPa)	Permeability K_1 (m^2)	Permeability K_2 (m^2)	Permeability K_3 (m^2)	Average permeability $\bar{K}$
2.5	1.0	1.47×10^{-17}	1.65×10^{-17}	1.22×10^{-17}	1.53×10^{-17}
2.5	2.0	8.90×10^{-18}	1.29×10^{-17}	9.90×10^{-18}	1.02×10^{-17}
2.5	3.0	8.57×10^{-18}	5.27×10^{-18}	1.05×10^{-17}	8.11×10^{-18}
2.5	4.0	7.12×10^{-18}	6.92×10^{-18}	7.75×10^{-18}	7.26×10^{-18}

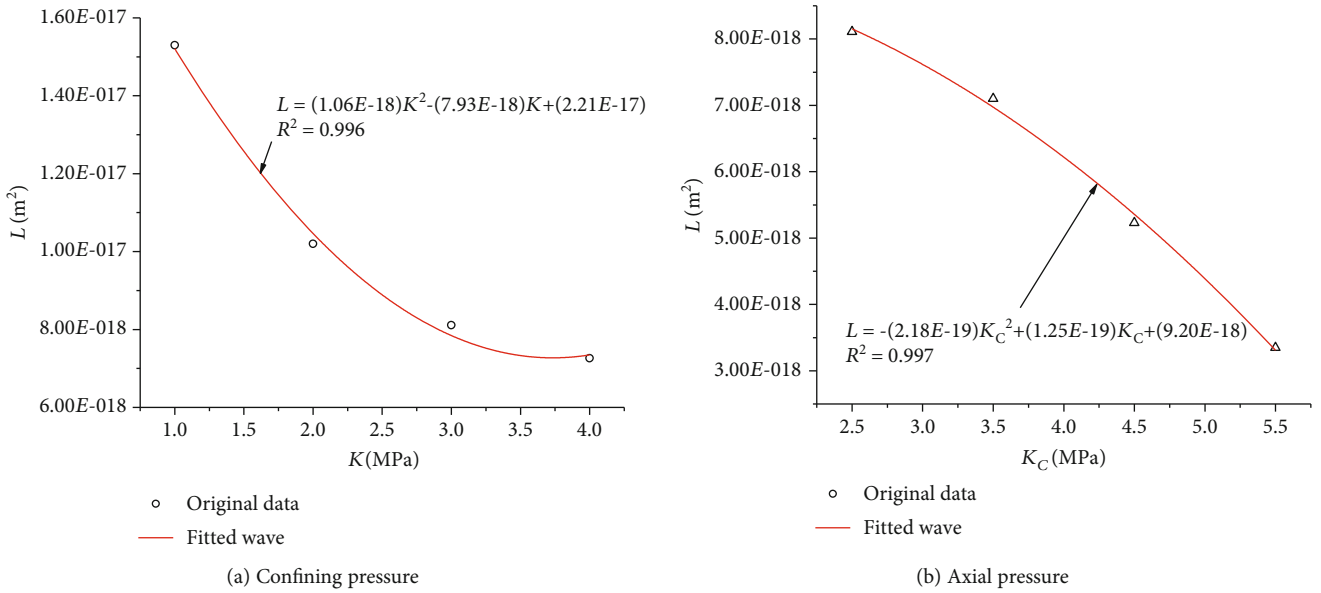

Figure 9: Permeability of SBCB under different stress states.

Table 3: Results of permeability testing of the SBCB under different axial pressures.

Axial pressure (MPa)	Confining pressure (MPa)	Permeability K_1 (m^2)	Permeability K_2 (m^2)	Permeability K_3 (m^2)	Average permeability $\bar{K}$
2.5	3.0	8.57×10^{-18}	5.27×10^{-18}	1.05×10^{-17}	8.11×10^{-18}
3.5	3.0	7.69×10^{-18}	6.67×10^{-18}	6.94×10^{-18}	7.10×10^{-18}
4.5	3.0	3.94×10^{-18}	7.52×10^{-18}	4.23×10^{-18}	5.23×10^{-18}
5.5	3.0	2.88×10^{-18}	2.84×10^{-18}	4.32×10^{-18}	3.35×10^{-18}

3.2. Influence Rules of Axial Pressure on the SBCB Permeability. The axial pressure effect on the permeability of the backfill was experimentally determined. During the experiment, a constant confining pressure of 3 MPa was applied, while the axial pressure was variable (2.5, 3.5, 4.5, and 5.5 MPa). Table 3 shows the SBCB permeability under different axial pressures. Figure 9(b) presents the best-fitting curve of SBCB permeability under different axial pressures. The permeability was related to the axial pressure via a quadratic polynomial, in which equation and correlation coefficient $R^2 = 0.997$ are given in Figure 9(b). As the axial pressure increased, the reduction amplitude of the permeability gradually grew. As the axial pressure increased from 2.5 to 5.5 MPa, the permeability dropped from 8.11×10^{-18} to 3.35×10^{-18} m^2, i.e., by 58.7%. This was because as the axial pressure increased, the pores inside the backfill were closed under compaction, resulting in a gradual decrease in permeability. Besides, the axial pressure direction was perpendicular to the seepage direction. As the axial pressure increased, the backfill specimens were compressed along the axial direction, thereby blocking the passage of water flow and accelerating the permeability reduction.

Under the action of confining pressure, the backfill was subjected to a transverse extruding force. The fractures' resulting compaction was slightly smaller than that exerted by the axial pressure on the backfill. Moreover, the confining pressure direction was parallel with the seepage direction, while the axial pressure direction was perpendicular to the

Table 4: Results of the orthogonal experiments on permeability.

Experiment No.	Axial pressure (MPa)	Confining pressure (MPa)	Permeability (m^2)
S1	2.5	3.0	8.11×10^{-18}
S2	3.5	3.0	7.10×10^{-18}
S3	4.5	3.0	5.23×10^{-18}
S4	5.5	3.0	3.35×10^{-18}
S5	2.5	1.0	1.53×10^{-17}
S6	2.5	2.0	1.02×10^{-17}
S7	2.5	4.0	7.26×10^{-18}

seepage direction. Thus, under different confining pressures, the fitted curve slope at the later stage was lower than the fitted curve's corresponding slope under different axial pressures.

3.3. Analysis of the Combined Effect of Multiple Factors. As shown by the above single-factor influence analysis, permeability's influencing factors mainly included confining pressure and axial pressure. In the goaf, the SBCB underwent a three-dimensional stress state. The permeability was influenced by both the confining pressure and axial pressure. An orthogonal experiment design was adopted to analyze multiple factors' combined effect on permeability to intuitively and accurately predict permeability's influence rules. The confining and axial pressures were taken as two influencing factors, each being allocated four levels. The orthogonal experiment design details and experimental results are listed in Table 4.

The range reflects the influence degree of different levels of various factors on the indicator of concern. The results of the orthogonal experiment in Table 4 were analyzed under each level of different factors. The results of range analysis of permeability under the combined action of different factors are summarized in Table 5.

It can be seen from Table 5 that the range of confining pressure was larger than that of the axial pressure. Different factors had a varying influence on the permeability of SBCB exposed to groundwater in the goaf. The confining pressure influenced the permeability of the backfill more significantly. The slope of the fitted curve of permeability in Figure 9(a) was considerably smaller than that of Figure 9(b). That is to say, the fitted curves of permeability under different stress states corresponded to the range analysis.

3.4. Influence Rules of Confining Pressure/Axial Pressure. The effect of different stress states (i.e., confining and axial pressures) on the backfill's permeability was analyzed in detail. The nephograms of permeability under different confining pressures/axial pressures were plotted based on the range analysis following the orthogonal experiment, as shown in Figure 10.

As indicated by the permeability isolines in Figure 10(a), the permeability was related to the confining/axial pressure in a roughly parabolic manner. The parabola's peak occurred under greater confining pressure, indicating that the confining pressure significantly influenced the backfill's permeability. According to Figure 10(b), with the confining pressure fixed at 0.5 MPa, the backfill's permeability varied less significantly as the axial pressure increased. When the confining pressure was increased to 2 MPa and then to 3 MPa, the permeability decreased considerably with the increasing axial pressure. This was because the backfill was subjected to larger axial and confining pressures simultaneously; both stresses acted on the backfill's contact surface within the range of elastic deformation. As a result, the backfill was densely compacted inside, leading to a more significant reduction in its permeability.

Table 5: Permeability range analysis.

Level	Axial pressure ($\times 10^{-18}$ Pa)	Confining pressure ($\times 10^{-18}$ Pa)
Level 1	10.2	15.3
Level 2	7.10	10.2
Level 3	5.23	5.95
Level 4	3.35	7.26
Range	6.85	9.35

4. Discussion

4.1. Analysis of the Seepage Mechanism of the SBCB under Different Confining Pressures. The influence of stress states on the SBCB permeability on the microscopic level was analyzed by preparing the SEM specimens after the seepage experiment under different stress states. The specimens' images under different stress states were magnified by the same factor, and their microstructure was observed via SEM.

Figure 11 shows the SEM patterns of the SBCB under different confining pressures. The particle size of the aeolian sand was the largest and varied between 168 and 571 μm. By contrast, fly ash and cement's particle sizes were smaller, with average values of 64.683 and 44.846 μm, respectively. Therefore, the fly ash and cement particles effectively filled the pores between the aeolian sand particles as aggregates. This structure offered greater compactness and smaller permeability of the backfill.

In Figure 11, the backfill specimens were all magnified by a factor of 5000 consistently. Under the confining pressure of 1 MPa (Figure 11(a)), many needle-/rod-like crystals appeared in the backfill. According to the XRD patterns, the needle-like crystals represented ettringite, which was relatively stable and contributed to the backfill's overall stability. After the hydration reaction, the fly ash was dispersed to form a gel, aggregated with the ettringite gel. The overall structure was loose, with many pores. Therefore, when confining pressure was 1 MPa at the early stage, the backfill's permeability was higher.

As the confining pressure increased to 3 and 4 MPa, as shown in Figures 11(c) and 11(d), a large amount of flocculated hydration product C-S-H was formed within the backfill. As the confining pressure continued to increase, the flocculated hydration product C-S-H overlapped in the middle of the backfill, increasing its compactness. Meanwhile, the

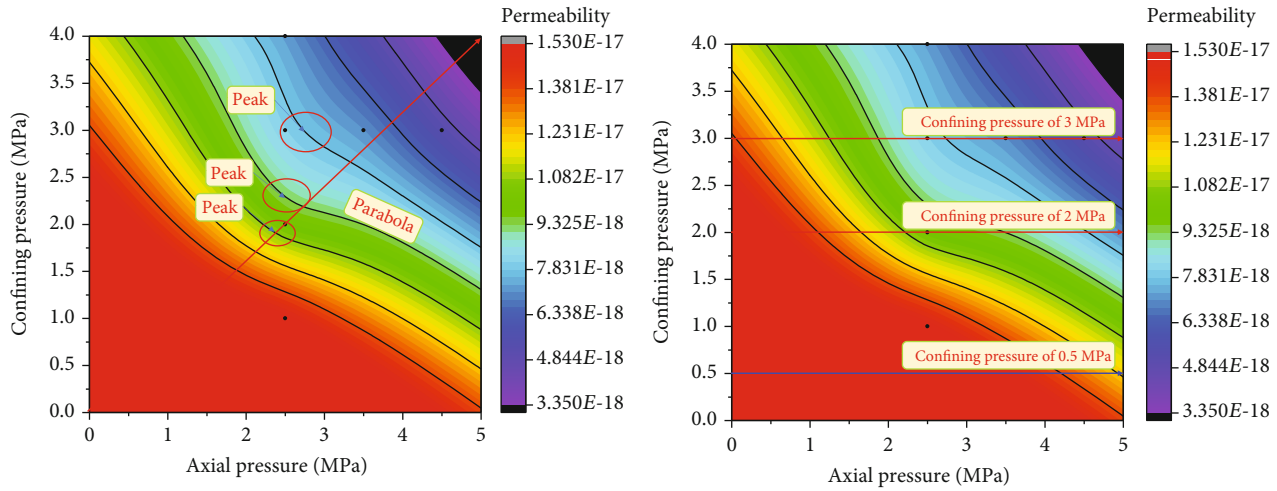

(a) Peak value of the parabola (b) Influence gradient

Figure 10: Influence of confining pressure/axial pressure on the SBCB permeability.

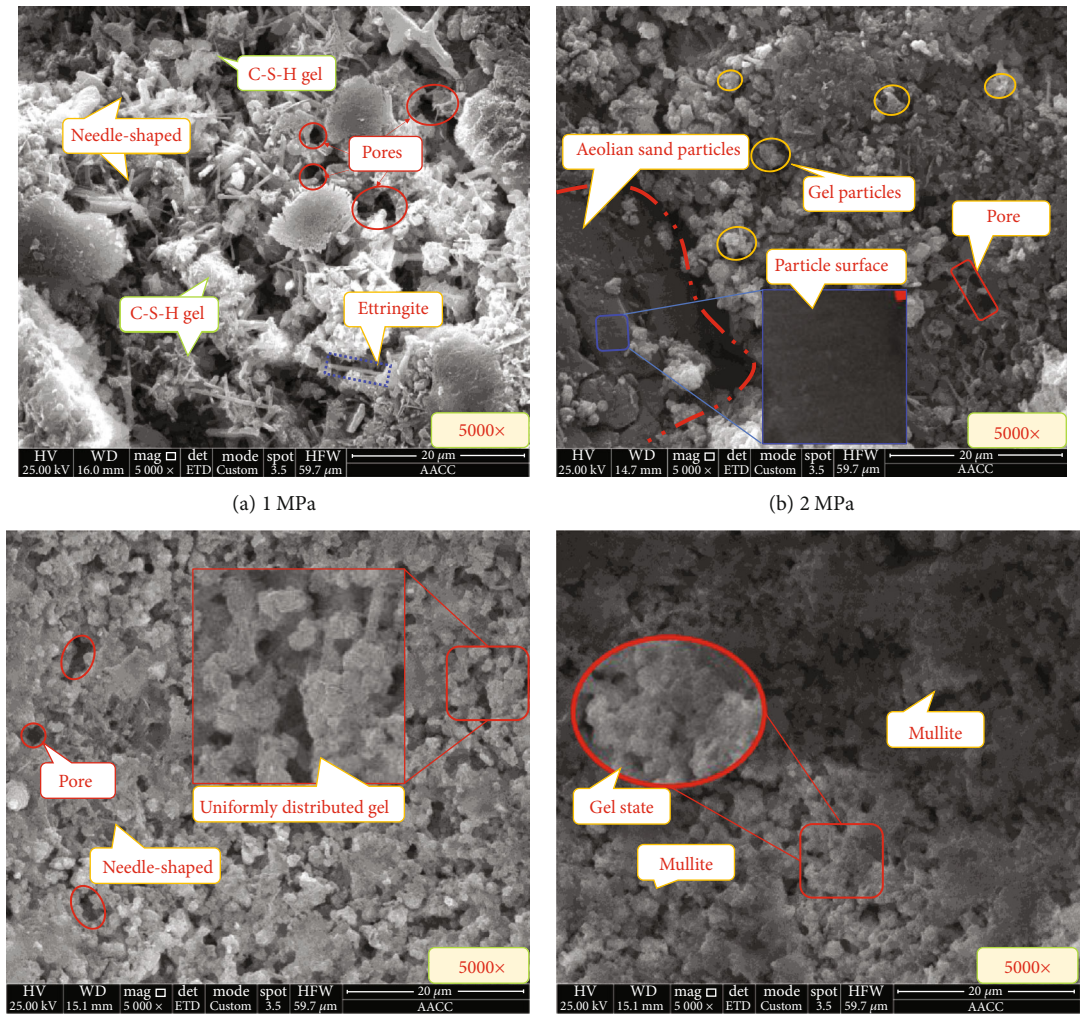

(a) 1 MPa (b) 2 MPa

(c) 3 MPa (d) 4 MPa

Figure 11: SEM patterns of SBCB under different confining pressures.

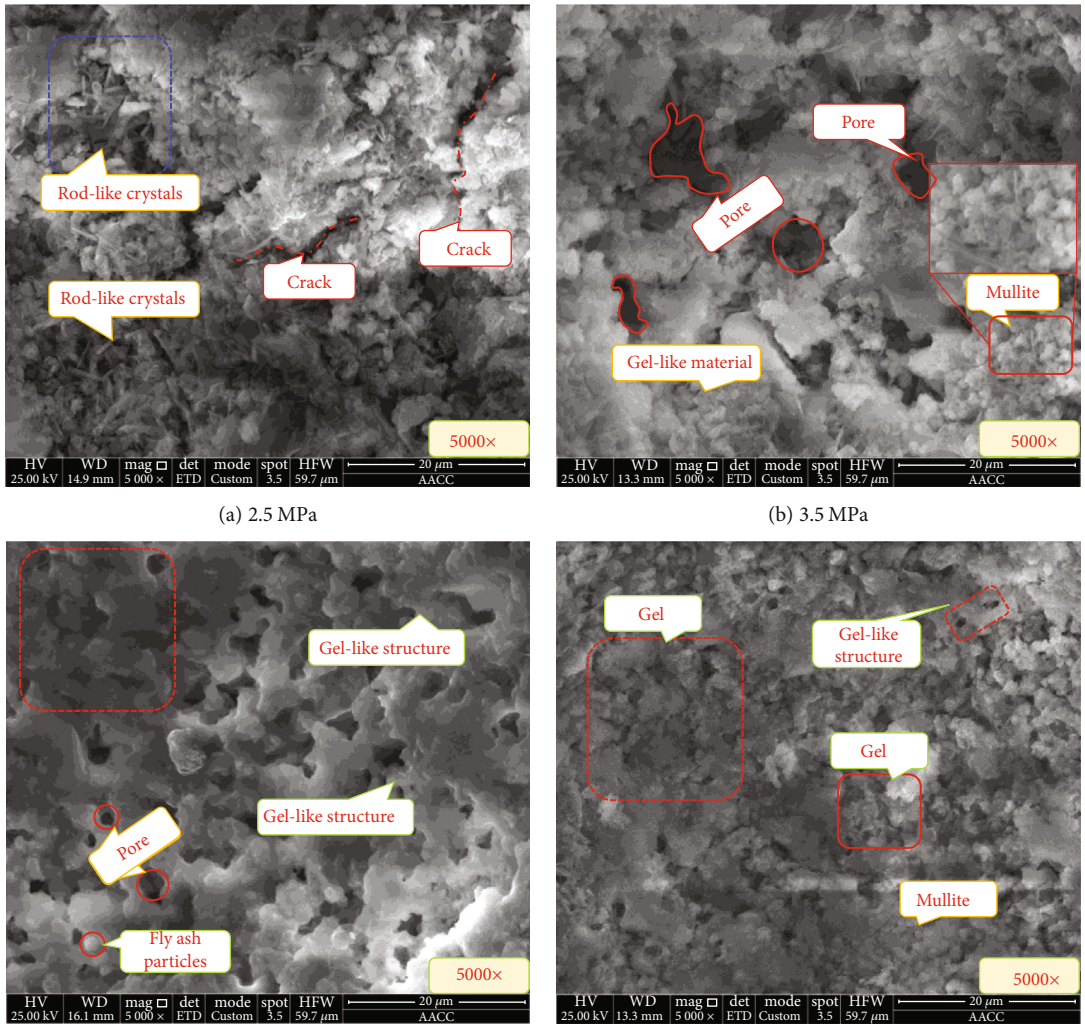

(a) 2.5 MPa

(b) 3.5 MPa

(c) 4.5 MPa

(d) 5.5 MPa

Figure 12: SEM patterns of the SBCB under different axial pressures.

number of needle-like crystals was considerably reduced. Therefore, the confining pressure had a more significant influence on the backfill's permeability.

4.2. Analysis of the Seepage Mechanism of the SBCB under Different Axial Pressures. The influence rules of axial pressure on the backfill's permeability were studied by comparing data for different confining pressures. Figure 12 shows the seepage mechanism of the SBCB under different axial pressures. The direction of axial pressure was parallel with the backfill's seepage direction, which was different from the case of the confining pressure. The direction of the axial pressure was perpendicular to the seepage direction of the backfill. This major distinction had a direct bearing on the seepage rules.

According to Figure 12, at the axial pressure of 2.5 MPa, more cracks appeared in the backfill, which was the major distinction from the confining pressure action. Moreover, a small amount of rod-like crystals, which were hydration products, appeared on the backfill particles' surface. The appearance of more cracks was mainly due to the loose structure within the backfill, which further led to a higher permeability at the early stage. As the axial pressure, which was perpendicular to the seepage direction, increased, the flocculated gel, as the fly ash's hydration product, was compressed vertically. The gel filled the pores between the backfill particles, reducing the porosity. Moreover, according to the XRD patterns shown in Figure 4, the aeolian sand contained many stable mineral components, such as quartz. Within the backfill, due to cement hydration and hardening at the early stage, fly ash was not involved in the hydration reaction and served as the filler between the cement particles, thus increasing the backfill's compactness.

Taken together, after the SBCB took shape, $Ca(OH)_2$ precipitated from cement due to hydration and was absorbed by the surfaces of fly ash particles. Meantime, the pozzolanic reaction proceeded as follows:

$$\begin{aligned} x\mathrm{Ca(OH)_2} + \mathrm{SiO_2} + n\mathrm{H_2O} &\rightarrow x\mathrm{CaO}\cdot\mathrm{SiO_2}\cdot(n+x)\mathrm{H_2O} \\ y\mathrm{Ca(OH)_2} + \mathrm{Al_2O_3} + n\mathrm{H_2O} &\rightarrow yx\mathrm{CaO}\cdot\mathrm{Al_2O_3}\cdot(n+y)\mathrm{H_2O} \end{aligned} \quad (2)$$

Fly ash and aeolian sand particles, acting as carriers, formed a flocculated gel by hydration reaction on the aeolian sand's particle surface. The flocculated gel tightly enveloped the aeolian sand particles to form a whole bulk, reducing the SBCB permeability.

5. Conclusions

A seepage system simulating the seepage mechanism of the SBCB was designed and tested. SBCB specimens were prepared with a fixed mix ratio. The backfill specimens' permeability and microstructure were studied under different stress states using a WAW-1000D series servohydraulic testing machine and SEM, respectively. The results obtained made it possible to draw the following conclusions:

(1) A particle size analyzer was employed to plot the normal distribution of the raw materials' particle size. The particle size of the aeolian sand ranged between 168 and 571 μm, with an average of 346.49 μm; that of the fly ash ranged from 19 to 126 μm, with an average of 64.683 μm; and that of the cement was between 6.9 and 99.3 μm, with an average of 44.846 μm. The XRD analysis revealed each raw material's mineral composition as the basis for subsequent macroscopic and microscopic studies of the backfill

(2) Permeability of the backfill specimens was studied under different confining pressures. The permeability was related to the confining pressure by a quadratic polynomial dependence. As the confining pressure increased, the permeability of the backfill gradually decreased. The confining pressure had a more significant influence on the permeability than the axial pressure. As the confining pressure increased from 1 to 4 MPa, the permeability dropped from 1.53×10^{-17} to 7.26×10^{-18} m^2, i.e., by 52.5%

(3) Permeability of backfill specimens was studied under different axial pressures. The permeability was related to the axial pressure by a quadratic polynomial dependence. As the axial pressure increased, the permeability decreased, at a progressively increasing rate. As the axial pressure increased from 2.5 to 5.5 MPa, the permeability decreased from 8.11×10^{-18} to 7.26×10^{-18} m^2, i.e., by 58.7%. The range of permeability under different confining and axial pressures was also analyzed. It was found that the confining pressure had a greater impact on the permeability of the backfill than the axial pressure

(4) The SBCB seepage mechanism under different stress states was investigated by SEM analysis. At small stresses, the backfill had a relatively loose structure and hence a higher permeability. As the stress increased, the flocculated gel C-S-H generated by the fly ash hydration at the later stage filled the pores between the aeolian sand particles, thus enhancing the backfill's compactness. The results of particle size analysis and XRD patterns confirmed that the confining pressure had a greater impact on the SBCB's permeability than the axial one

Data Availability

The latest data used to support the findings of this study are included within the article.

Conflicts of Interest

The authors declare that they have no conflicts of interest.

Acknowledgments

This study was financially supported by the National Key R&D Program of China (grant number 2018YFC0604706), the National Natural Science Foundation of China (grant number 51874287), and the Independent Research Project of State Key Laboratory of Coal Resources and Safe Mining, CUMT (grant number SKLCRSM19X006).

References

[1] D. Y. Zhang, W. H. Sui, and J. W. Liu, "Overburden failure associated with mining coal seams in close proximity in ascending and descending sequences under a large water body," *Mine Water and the Environment*, vol. 37, no. 2, pp. 322–335, 2018.

[2] D. B. Wang, X. B. Bian, H. Qin, D. L. Sun, and B. Yu, "Experimental investigation of mechanical properties and failure behavior of fluid-saturated hot dry rocks," *Natural Resources Research*, vol. 30, no. 1, pp. 289–305, 2021.

[3] L. L. Xiao, Q. Wu, C. Niu et al., "Application of a new evaluation method for floor water inrush risk from the Ordovician fissure confined aquifer in Xiayukou coal mine, Shanxi, China," *Carbonate Evaporite*, vol. 35, no. 3, article 97, 2020.

[4] M. L. Hu, W. L. Zhao, Z. Lu, J. X. Ren, and Y. P. Miao, "Research on the reasonable width of the waterproof coal pillar during the mining of a shallow coal seam located close to a reservoir," *Advances in Civil Engineering*, vol. 2019, Article ID 3532784, 14 pages, 2019.

[5] D. Ma, J. J. Wang, and Z. H. Li, "Effect of particle erosion on mining-induced water inrush hazard of karst collapse pillar," *Environemental Science and Pollution Research*, vol. 26, no. 19, pp. 19719–19728, 2019.

[6] L. Q. Ma, X. Du, F. Wang, and J. M. Liang, "Water-preserved mining technology for shallow buried coal seam in ecologically-vulnerable coal field: a case study in the Shendong coal field of China," *Disaster Advances*, vol. 6, pp. 268–278, 2013.

[7] Y. Suo, Z. Chen, S. S. Rahman, and H. Song, "Experimental and numerical investigation of the effect of bedding layer orientation on fracture toughness of shale rocks," *Rock Mechanics and Rock Engineering*, vol. 53, no. 8, pp. 3625–3635, 2020.

[8] D. B. Wang, Y. C. Dong, D. L. Sun, and B. Yu, "A three-dimensional numerical study of hydraulic fracturing with degradable diverting materials via CZM-based FEM," *Engineering Fracture Mechanics*, vol. 237, article 107251, 2020.

[9] W. B. Sun, Y. Wang, H. F. Qiu, and Z. W. Ding, "Numerical simulation study of strip filling for water-preserved coal

mining," *Environemental Science and Pollution Research*, vol. 27, no. 12, pp. 12899–12907, 2019.

[10] Q. Sun, J. X. Zhang, N. Zhou, and W. Y. Qi, "Roadway backfill coal mining to preserve surface water in Western China," *Mine Water and the Environment*, vol. 37, no. 2, pp. 366–375, 2018.

[11] X. J. Deng, J. X. Zhang, N. Zhou, B. de Wit, and C. T. Wang, "Upward slicing longwall-roadway cemented backfilling technology for mining an extra-thick coal seam located under aquifers: a case study," *Environment and Earth Science*, vol. 76, no. 23, p. 789, 2017.

[12] N. Zhou, J. X. Zhang, S. Y. Ouyang, X. J. Deng, C. W. Dong, and E. B. Du, "Feasibility study and performance optimization of sand-based cemented paste backfill materials," *Journal of Cleaner Production*, vol. 259, p. 120798, 2020.

[13] X. P. Shao, L. Wang, X. Li et al., "Study on rheological and mechanical properties of aeolian sand-fly ash-based filling slurry," *Energies*, vol. 13, no. 5, p. 1266, 2020.

[14] J. Li, S. Q. Zhang, Q. Wang et al., "Feasibility of using fly ash–slag-based binder for mine backfilling and its associated leaching risks," *Journal of Hazardous Materials*, vol. 400, p. 123191, 2020.

[15] J. P. Qiu, Y. L. Zhao, J. Xing, and X. G. Sun, "Fly ash/blast furnace slag-based geopolymer as a potential binder for mine backfilling: effect of binder type and activator concentration," *Advances in Materials Science and Engineering*, vol. 2019, Article ID 2028109, 12 pages, 2019.

[16] X. J. Deng, Z. X. Yuan, L. X. Lan, B. de Wit, and J. W. Zhang, "Roof movement and failure behavior when mining extra-thick coal seams using upward slicing longwall-roadway cemented backfill technology," *Advances in Materials Science and Engineering*, vol. 2020, Article ID 5828514, 15 pages, 2020.

[17] H. F. Liu, J. X. Zhang, B. Y. Li et al., "Environmental behavior of construction and demolition waste as recycled aggregates for backfilling in mines: leaching toxicity and surface subsidence studies," *Journal of Hazardous Materials*, vol. 389, p. 121870, 2020.

[18] Q. Sun, J. X. Zhang, W. Y. Qi, and M. Li, "Backfill mining alternatives and strategies for mitigating shallow coal mining hazards in the Western mining area of China," *Quarterly Journal of Engineering Geology and Hydrogeology*, vol. 53, no. 2, pp. 217–226, 2020.

[19] W. Y. Qi, Y. L. Huang, H. He, J. X. Zhang, J. M. Li, and M. Qiao, "Potential pollution of groundwater by dissolution and release of contaminants due to using gangue for backfilling," *Mine Water and the Environment*, vol. 38, no. 2, pp. 281–293, 2019.

[20] H. F. Liu, J. X. Zhang, W. Q. Zhang, F. Gao, H. Yan, and T. L. An, "Experimental investigation of perceptual characteristics of functional cemented backfilling materials in coal mines," *Minerals*, vol. 9, no. 1, p. 55, 2019.

[21] W. Y. Qi, J. X. Zhang, and Q. Zhang, "Compression of aggregates of acid-leached coal gangues: implications for coal mine backfill," *Advances in Materials Science and Engineering*, vol. 2018, Article ID 7056430, 13 pages, 2018.

[22] R. L. Zhang, L. N. Ma, P. Liu et al., "Influence mechanisms under different immersion methods and different strengths of concrete in corrosive environments, and verification via long-term field test," *Structural Concrete*, vol. 21, no. 5, pp. 1853–1864, 2020.

[23] Q. Sun, J. X. Zhang, and N. Zhou, "Early-age strength of aeolian sand-based cemented backfilling materials: experimental results," *Arabian Journal For Science And Engineering*, vol. 43, no. 4, pp. 1697–1708, 2018.

[24] C. Zhu, X. D. Xu, W. R. Liu et al., "Softening damage analysis of gypsum rock with water immersion time based on laboratory experiment," *IEEE Access*, vol. 9, pp. 125575–125585, 2019.

[25] D. Ma, J. X. Zhang, H. Y. Duan et al., "Reutilization of gangue wastes in underground backfilling mining: overburden aquifer protection," *Chemosphere*, vol. 264, article 128400, 2020.

[26] X. Y. Liu, Z. D. Zhu, and A. H. Liu, "Permeability characteristic and failure behavior of filled cracked rock in the triaxial seepage experiment," *Advances in Civil Engineering*, vol. 2019, Article ID 3591629, 12 pages, 2019.

[27] J. Mamaghanian, B. V. S. Viswanadham, and H. R. Razeghi, "Centrifuge model studies on geocomposite reinforced soil walls subjected to seepage," *Geosynthetics International*, vol. 26, no. 4, pp. 371–387, 2019.

[28] J. F. Hou, Z. P. Guo, W. Z. Liu, H. Z. Yang, and W. W. Xie, "Study on damage model and damage evolution characteristics of backfill with prefabricated fracture under seepage-stress coupling," *Advances in Materials Science and Engineering*, vol. 2020, Article ID 3642356, 2020.

[29] P. J. Santos and P. L. A. Barros, "Active earth pressure due to soil mass partially subjected to water seepage," *Canadian Geotechnical Journal*, vol. 52, no. 11, pp. 1886–1891, 2015.

[30] J. F. Hou, Z. P. Guo, W. Z. Liu, and Y. X. Zhang, "Mechanical properties and meso-structure response of cemented gangue-fly ash backfill with cracks under seepage- stress coupling," *Construction and Building Materials*, vol. 250, p. 118863, 2020.

[31] P. L. A. Barros and P. J. Santos, "Coefficients of active earth pressure with seepage effect," *Canadian Geotechnical Journal*, vol. 49, no. 6, pp. 651–658, 2012.

[32] X. B. Zhang, H. H. Chen, C. Yao et al., "Seepage characteristics of triaxial compression-induced fractured rocks under varying confining pressures," *International Journal of Geomechanics*, vol. 20, no. 9, article 04020160, 2020.

[33] C. Y. Zhou, L. Yu, F. F. You, Z. Liu, Y. H. Liang, and L. H. Zhang, "Coupled seepage and stress model and experiment verification for creep behavior of soft rock," *International Journal of Geomechanics*, vol. 20, no. 9, article 04020146, 2020.

[34] N. Zhou, H. B. Ma, S. Y. Ouyang, D. Germain, and T. Hou, "Influential factors in transportation and mechanical properties of aeolian sand-based cemented filling material," *Minerals*, vol. 9, no. 2, p. 116, 2019.